Theoretical and Applied Fracture Mechanics 145 (2026) 105617

Contents lists available at ScienceDirect

Theoretical and Applied Fracture Mechanics

journal homepage: www.elsevier.com/locate/tafmec

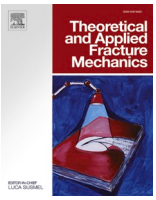

How differences in fracture process zone behavior prevent transferability of mixed-mode fracture toughness measurements in toughened adhesive CFRP joints

Ishan Manoj *, Daniel Bernardes de Castro, John-Alan Pascoe, René Alderliesten

Aerospace Structure and Materials, Delft University of Technology, 2600 GB Delft, The Netherlands

ARTICLE INFO

Keywords:
Fracture process zone
Strain energy release rate
Compliance
Damage evolution
Mode-dependence
Digital image correlation
Finite element analysis

ABSTRACT

The fracture process zone (FPZ) significantly influences the damage tolerance of adhesively bonded composite joints, governing crack-growth mechanisms and migration. Existing fracture characterization approaches generally evaluate pure-mode behavior independently and extend these results to mixed-mode conditions using a power-criterion, such as the Benzeggagh-Kenane (B–K) criterion. This process assumes that FPZ-dependent mode-mix behavior from a standard mixed-mode test is transferable to another complex loading condition. This assumption remains unchecked for toughened adhesive joints, where FPZ morphology varies with loading conditions.

This study addresses this gap through experimental and numerical investigation using digital image correlation (DIC) and cohesive zone modeling (CZM). The pure mode I test displayed localized FPZ ahead of the crack tip, influenced by carrier bridging. Two different pure Mode II tests demonstrated that the apparent crack length method accurately accounts for the large FPZ ahead of the crack tip. The mixed-mode bending (MMB) test linked pure modes through the B–K criterion. The Crack-Lap Shear (CLS) specimens exhibited evolving FPZ and mode II-dominated fracture.

The fracture toughness predicted by the B–K criterion deviated from the CLS tests as the loading became more mode II dominant. It was observed that the FPZ morphology during the CLS test differed significantly from that observed during the MMB test, through DIC and CZM. These results highlight that differences in FPZ affect the mixed-mode fracture toughness and demonstrate the limitations of applying a single empirical power-criterion. It underscores for FPZ-sensitive approaches to accurately predict the fracture resistance of toughened adhesive joints under evolving mixed-mode conditions.

1. Introduction

Adhesive joints are being used increasingly in modern aerospace, automotive, and industrial applications because they offer significant design flexibility compared to conventional joining techniques [1,2]. Other advantages include a reduction in overall structural weight, minimal damage to the substrate, and improved stress distribution across the joint interface [3,4]. Improvement in adhesive joint properties and achieving stable crack growth have been central themes in theoretical, experimental, and applied research over several years [5]. Factors, including loading conditions under different mode-mixities, specimen compliance, strain energy release rate (SERR) of the adhesive, interlaminar strength, and fiber bridging, have been identified as playing a pivotal role in assessing the mechanical behavior and failure mechanisms of adhesive joints [6,7].

Any structural component, when loaded, undergoes a pure or mixed mode of loading. This loading deforms the joint interface, which induces stresses in the joints [8,9]. This complex non-uniform stress distribution across the joint interface generates a fracture process zone (FPZ), which governs the crack growth and its stability [10,11]. The magnitude and evolution of FPZ are primarily dictated by the relative contributions of induced in-plane shear or peeling stress, which vary across the bond-layer. Typically, bonded joints exhibit a higher resistance to in-plane shear deformation (Mode II) compared to out-of-plane stress (peeling stress or Mode I) [12,13]. Consequently, bonded joints are designed to maximize in-plane shear loading and minimize peeling stress [14,15].

* Corresponding author.
E-mail address: i.manoj@tudelft.nl (I. Manoj).

https://doi.org/10.1016/j.tafmec.2026.105617
Received 26 January 2026; Received in revised form 19 March 2026; Accepted 3 April 2026
Available online 6 April 2026

These complex stresses across the joint interface, which dictate the FPZ, are heavily influenced by the specimen compliance, as it determines the joint deformation behavior [16]. The analysis of the FPZ in predicting disbond behavior and achieving stable crack growth becomes more complex when the substrate is compliant and susceptible to high deformation [17–19]. The challenges in properly evaluating the FPZ to accurately estimate the strain energy release rate (SERR) further intensify when joints are bonded with tough adhesives, such as AF163-2K, due to the formation of a large apparent crack length ahead of the crack tip [20,21]. Additionally, the interaction between FPZ development and the SERR of the adhesive, as well as the interlaminar strength of the adherend, governs crack growth in the bond layer or potential crack migration into the composite adherends [22–24]. Moreover, extrinsic toughening mechanisms, such as carrier bridging, also influence the FPZ formed ahead of the crack tip [25]. Hence, it follows that the damage tolerance of adhesively bonded composite joints is strongly dependent on the evolution of the FPZ [26,27]. It becomes imperative to consider FPZ evolution based on different mode mixities, specimen compliance, extrinsic toughening mechanisms, and accurate estimation of apparent crack length to reliably interpret the different mixed-mode behavior in toughened bonded joints [28–31].

The majority of existing studies correlate measured pure-mode behaviors with mixed-mode behavior using power-criterion relations, such as the Benzeggagh-Kenane (B–K) criterion. Additionally, the mode-mixity effects are commonly accounted for by the mixed-mode bending (MMB) test [13,32–34]. This practice implicitly assumes that the mode-mixity dependence observed in one test is transferable to other mixed-mode conditions. Yet, for toughened adhesive joints that develop large, mode-dependent FPZs, this assumption remains unverified [35]. A noticeable gap exists in the literature regarding the transferability of empirical fracture criteria across different specimen geometries. Specifically, a B–K curve derived from standard MMB tests may not reliably predict disbond behavior in specimens like the CLS, where the FPZ evolves differently due to the inherent mode-mixity and geometry. Even if the FPZ is accounted for during initial pure-mode characterization, the assumption that mixed-mode toughness follows a fixed empirical path overlooks the configuration-dependent nature of the process zone. This highlights an uncertainty that a single empirical power criterion can substitute a detailed characterization of the FPZ as the loading condition varies and mode-mixity evolves. Hence, the limitations of the current power criterion motivate the development of models that are sensitive to the evolution of the FPZ under complex loading. The mode mixity evolution dictated by the FPZ should be extended to more practical loading conditions, like the Cracked Lap Shear (CLS) Test [36–38]. Hence, the conjunction of different mode mixity configurations with the pure modes test is essential to developing a comprehensive and unified understanding of the failure mechanism [19,28,39,40].

The objective of the present study was to investigate the extent to which a B–K mixed-mode fracture criterion, determined from pure mode tests and one mixed-mode test, can be applied to correctly predict the fracture toughness for a different mixed-mode test, with a different FPZ configuration. This was done by systematically evaluating the failure mechanism in Carbon Fiber Reinforced Polymer (CFRP) joints bonded with the toughened adhesive AF163-2K under various loading conditions. Experimentation involved five different test configurations, including pure Mode I DCB tests, pure Mode II Calibrated End-load Split (CELS) tests, 3-point bending End-Notch Flexural (ENF) tests, and mixed-mode tests including MMB and CLS tests. These tests collectively present a comprehensive framework for assessing the FPZ, combining the effects of specimen compliance, apparent crack length, mode mixity, and carrier bridging. The DCB, ENF, and MMB methods used to establish the fracture envelope under constant mode ratios do inherently guarantee Self-Similar Crack Propagation (SSCP); the CLS specimen does not inherently guarantee SSCP. The MMB and CLS tests demonstrate a rigorous distinction between fracture characterization and structural applications. In aerospace certification, it is common practice to use coupon-level benchmarks (DCB/ENF/MMB) to assess performance at the element or "large structure" level [26,27]. The CLS provides a unique environment to study the "transferability" of properties from idealized, self-similar tests to complex, Mode II-dominant structural geometries.

Initially, fracture characterization was carried out for pure mode I and II tests to characterize the adhesive's intrinsic toughness (Fig. 1). Additionally, the FPZ was accounted for by using data reduction schemes and was correlated with a computational model to build confidence in the analysis. Subsequently, a mixed-mode bending test was performed to establish a power-criterion criterion that sums up individual SERR components to the critical SERR. This power-criterion criterion was compared with a CLS configuration using a different mode mixture, enabling an investigation of the evolution of FPZ across varying mode mixtures.

2. Materials and methodology

The experimental methodology and specimen configurations were designed in accordance with well-established guidelines for delamination characterization in fiber-reinforced composites, as no specific standardized procedures currently exist for adhesively bonded joints. Mode I DCB tests were performed following the ASTM D5528 standard [41], while Mode II ENF and CELS tests were conducted in accordance with ASTM D7905 and ISO 15114, respectively [42,43]. AF 163-2K is an epoxy structural film adhesive known for its high peel and shear strength. Moreover, it is easy to handle and has a simple manufacturing and curing process. It is supported by a knit carrier, which helps in maintaining uniform bond-line thickness. Adhesive AF163-2K has shown considerable variability in its reported mode II fracture properties across the literature [44–51]. To capture this variability, two different Mode II configurations were employed to understand the role of FPZ in determining the critical strain energy release rate, G_{IIC} [52,53].

Several data reduction schemes in the literature calculate the fracture resistance from experimental data tests of CELS and ENF specimens. Classical data reduction approaches, such as Corrected Beam Theory (CBT) and Compliance Calibration Method (CCM), rely on the real-time, accurate measurement of the physical crack length during propagation. However, these methods are highly sensitive to experimental error and subjective interpretation, as identifying the precise location of the crack tip under Mode II loading is inherently difficult [54,55]. This challenge is further exacerbated by the development of large FPZs, which are only marginally captured by conventional methods [52,56].

Given that the focus of the present work is the evolution of the FPZ on fracture resistance rather than a comparison of data reduction methodologies, the apparent crack length method was exclusively utilized [57–59]. The apparent crack length methods are widely regarded as a

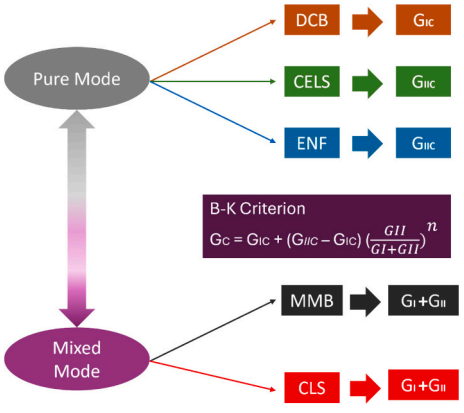

Fig. 1. Framework developed to link pure and mixed-mode behavior through experimental and computational studies.

robust and reliable scheme because they circumvent the need for direct crack length monitoring [60–62]. The reader is referred to the appendix for details on data reduction schemes. The apparent crack length methods show less repeatability scatter, and hence a smaller sample size is required.

Mixed-mode characterization was performed using the MMB configuration at a 50:50 Mode I/II ratio, as specified in ASTM D6671 [63]. For MMB tests, the sample size was increased proactively to mitigate the greater sensitivity of mixed-mode loading to slight alignment variations and to ensure a statistically significant mean. Although no standardized test procedure currently exists for the CLS configuration, a reliable and repeatable test protocol was adopted based on the experimental procedures reported by Brussat et al. [64] and Barros et al. [37,40], as discussed in detail in the upcoming sections. DCB and CLS tests were monitored in real time via optical tracking; the high visibility of the crack tip in these specimens enabled greater precision with fewer repetitions.

2.1. Manufacturing

The adherends were fabricated using HexPly IM7/8552 unidirectional carbon fiber/epoxy prepreg with a nominal fiber volume fraction of approximately 57.7% (as per data sheet) [65]. HexPly IM7/8552 comprises IM7, an intermediate-modulus carbon fiber with high tensile strength and stiffness. Matrix 8552 is a toughened epoxy resin that does not flow excessively during curing, ensuring a high fiber volume percentage.

Each adherend consisted of 16 plies oriented in the 0° direction, aligned with the longitudinal axis of the specimens. The unidirectional alignment concentrates energy release at the adhesive interface, preventing the crack from easily migrating into the composite plies, which is essential for studying the evolution of the FPZ. 16 layers were used as the desired thickness of each arm "h" $\approx 2.16 \pm 0.09$ mm was achieved, to ensure the adherends were stiff enough to remain elastic during testing. The average laminate thickness was measured at five locations on each side of the cured laminates. The prepreg sheets were cut and stacked according to the planned lay-up sequence and consolidated using a hand lay-up process with vacuum debulking applied after each alternate ply. The adherend length was maintained as specified for the test requirements (see Section 2.3). The specimen width for all test configurations was fixed at 25 mm to ensure consistency in comparison. The laminates were cured in an autoclave following the manufacturer's recommended temperature and pressure cycle at an absolute pressure of 7 bar and a maximum temperature of 180 °C for 7 h [65]. Following post-curing, a C-scan inspection was conducted to verify laminate quality and detect any internal defects.

The cured laminates were precisely trimmed to the desired geometry using a Comp-Cut cutting machine, using a cutting disc and water as a coolant, before being bonded together. Surface preparation of the adherends involved light abrasion with P120-grade sandpaper along the fiber direction, followed by cleaning with isopropanol using lint-free cotton cloths [66]. The upper and lower adherends were bonded using the structural film adhesive AF163-2K. Initial pre-cracks for each specimen type were introduced using a thin Teflon insert (≈0.1 mm), as described in Section 3. The assembled joints were cured again in the autoclave following the adhesive manufacturer's recommended curing cycle [67]. The composite joints were cut from the bonded laminate to the final specimens. The average adhesive layer thickness, measured under an optical microscope after curing, was approximately 0.17 ± 0.02 mm.

End blocks for the DCB, CELS, and MMB specimens were grit-blasted and cleaned with acetone prior to bonding. For CLS specimens, tapered glass fiber-reinforced polymer (GFRP) tabs were used to prevent local crushing under high clamping forces, as a pressure of 175 bar was required to minimize slippage during testing [51]. All end blocks and tabs were bonded with Loctite EA 3425 and allowed to cure at room temperature for 48 h. A minimum of three specimens for each test configuration were fabricated to ensure repeatability of results.

2.2. Experimental set-up

The DCB, ENF, CELS, and MMB tests were conducted using a Zwick universal testing machine equipped with either a 1 kN or 10 kN load cell, depending on the expected load range. The CLS tests were performed on a separate Zwick testing machine equipped with a 250 kN load cell, which accommodates the higher failure loads associated with these configurations, as discussed later. All tests were performed under displacement-controlled conditions at a quasi-static loading rate of 0.5 mm/min. Representative test setups for the MMB, DCB, and CLS configurations are shown in Fig. 2.

A high-resolution camera was positioned on one lateral side of the specimen to monitor crack initiation and propagation throughout the tests. This lateral side of specimens was coated with a thin white paint layer, and reference markers were inscribed using a fine-tipped (≈0.1 mm) knife at uniform intervals to facilitate visual crack tracking. Simultaneously, a high-resolution camera was used on the opposite side of the specimen to record the deformation field [68,69]. A fine stochastic speckle pattern was applied to this surface to enable accurate strain mapping and analysis via digital image correlation (DIC). The DIC system (Vic 3D) provided full-field strain and displacement maps, while the visual camera offered complementary information on crack growth, enabling precise measurement of disbond propagation. For the CLS configuration, 3D DIC was employed to capture potential out-of-plane deformation, with proper calibration conducted prior to testing.

Additionally, a third high-resolution camera was mounted to monitor the displacement and rotation of the end blocks connected to the testing machine during the DCB, CELS, MMB, and ENF tests. This setup allowed for the correction of any kinematic discrepancies in the displacement readings.

All imaging systems were synchronized with the controller of the testing machine to correlate force and displacement data with the visual and DIC records. Crack-tracking and DIC images were captured at intervals of 1–3 s, while the end-block motion camera recorded at 5–10 s intervals. Adequate illumination was provided throughout testing to minimize the influence of ambient light variability. All experiments were carried out under ambient laboratory conditions at 22 °C and 60% relative humidity.

2.3. Methodology and geometric details

2.3.1. Mode I – double cantilever beam test

The opening mode DCB test was performed to determine the pure mode I fracture toughness (G_{IC}) [70]. The geometric dimensions and test specimen for the DCB test are illustrated in Fig. 3. The initial crack length "a_0" for the DCB samples was ≈66 ± 1 mm, whereas the thickness of each arm "h" was ≈2.16 ± 0.09 mm. The end block was attached to load the specimens. The Modified Beam Theory (MBT) was used for data reduction (see appendix). To gain more insight into the variability induced by data post-processing, the tests were analyzed by two independent observers.

2.3.2. Mode II – calibrated end-load split

CELS specimens were fabricated with an initial crack length "a_0", measured from the loading point, of 60 ± 1 mm (Fig. 4). Mode II pre-cracking was performed at a displacement rate of 0.5 mm/min, followed by unloading at a rate of 5 mm/min, as recommended in ISO 15114 [42]. The initial free length for pre-cracking was selected to satisfy a ratio of $a_0/L \approx 0.8$, resulting in a relatively short span. Crack extension was confined within the 2–5 mm range, and 2.5 mm markings were inscribed along the specimen edge. The pre-cracking process was terminated once the crack front advanced beyond the first marking and slightly before the second, yielding a new effective pre-crack length of

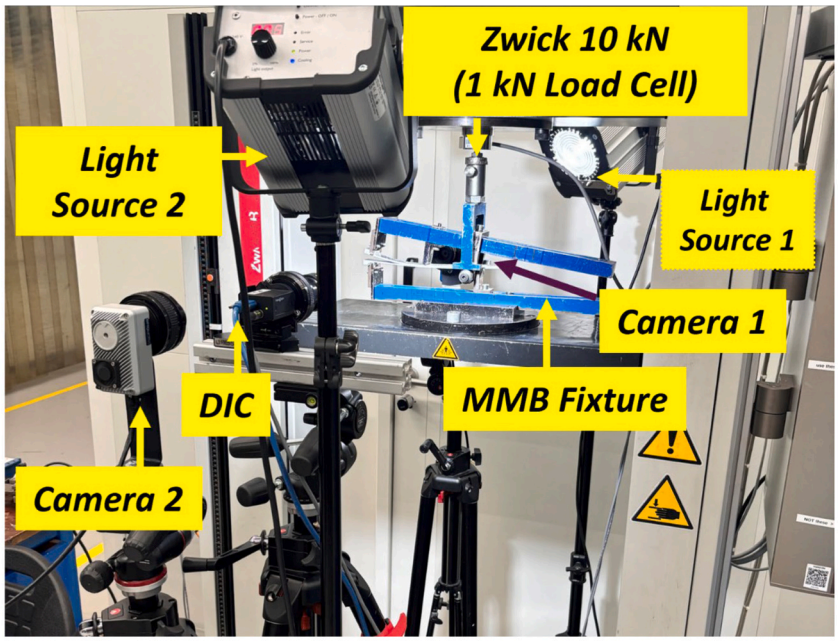

(a)

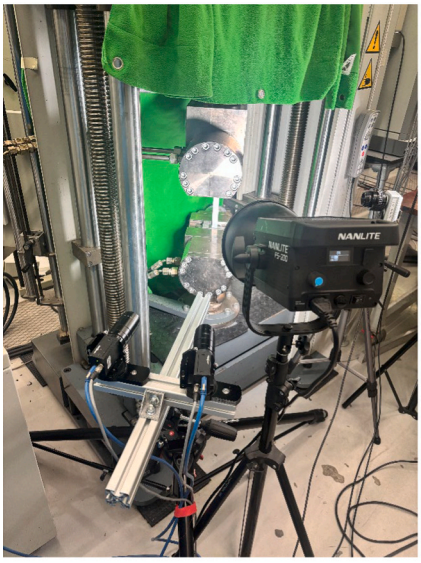

(b)

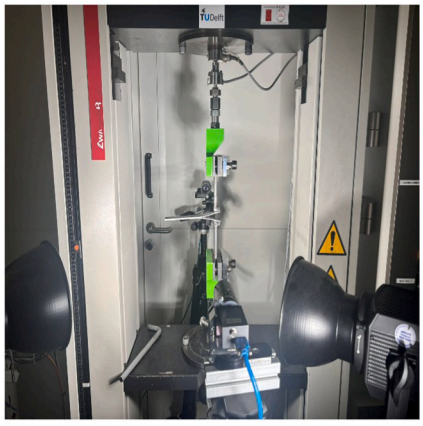

(c)

Fig. 2. Experimental test set-up for different configurations using DIC, high-resolution cameras, and Zwick Machines (a) MMB, (b) CLS, (c) DCB.

approximately 63.5 ± 1.5 mm, as confirmed through visual inspection. For the final fracture tests, a longer free length ($L \approx 95$ *mm*) was employed to ensure a fully developed R-curve, corresponding to a ratio of "$a_P/L \approx 0.66$". The Corrected Beam Theory with Effective Crack Length (CBTE) method was employed as the primary data reduction approach to evaluate G_{IIC} (see appendix).

2.3.3. Mode II – 3 point bending end-notch flexure

A three-point bending ENF test was performed to compare the pure mode II results with those of the CELS specimens, taking into account any variations that may arise due to differences in test configuration [52,71]. The initial crack length introduced by the Teflon insert was 70 mm.

The span length between the two bottom rollers was set to "$2L = 100$ *mm*", in accordance with ASTM D7905 [43], with a distance of 50 mm maintained between the consecutive rollers (Fig. 5). The initial crack length, a_0, measured from the first bottom roller to the crack tip, was approximately 30 ± 1 mm. The Compliance Beam Calibration Method with apparent crack length (CBBM) method was employed as the primary data reduction approach to evaluate G_{IIC} for ENF, due to its reliability as reported in literature [52,60–62,72] (see Appendix).

2.3.4. Mixed-mode bending (50:50)

The MMB test was carried out to characterize the adhesive under mixed loading conditions [13]. The mode mix chosen for the test was 50:50 mode I/mode II. The initial crack length "a_0" for the MMB test was ≈64 ± 1 mm, and the total span length "$2L$" for the specimen was 200 mm (Fig. 6). Loading blocks were bonded to the specimen to clamp the lower arm and apply a load on the upper arm. In this study, the fracture envelope was defined using these standardized methods to ensure a stable FPZ. While additional MMB ratios (e.g., 20:80 or 80:20) could have been performed, in this study, the mixed-mode characterization

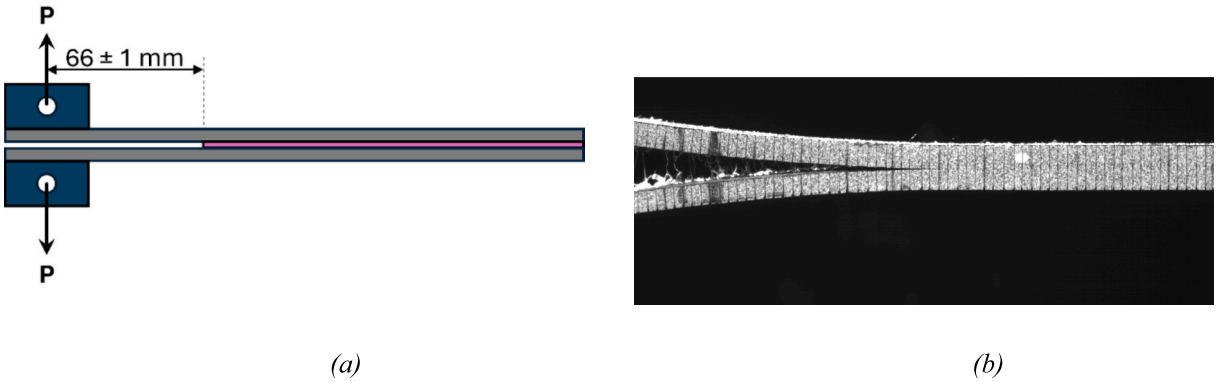

Fig. 3. (a) Schematic representation of DCB samples (figure not to scale), (b) carrier bridging happening during crack propagation for Mode I opening, captured by camera.

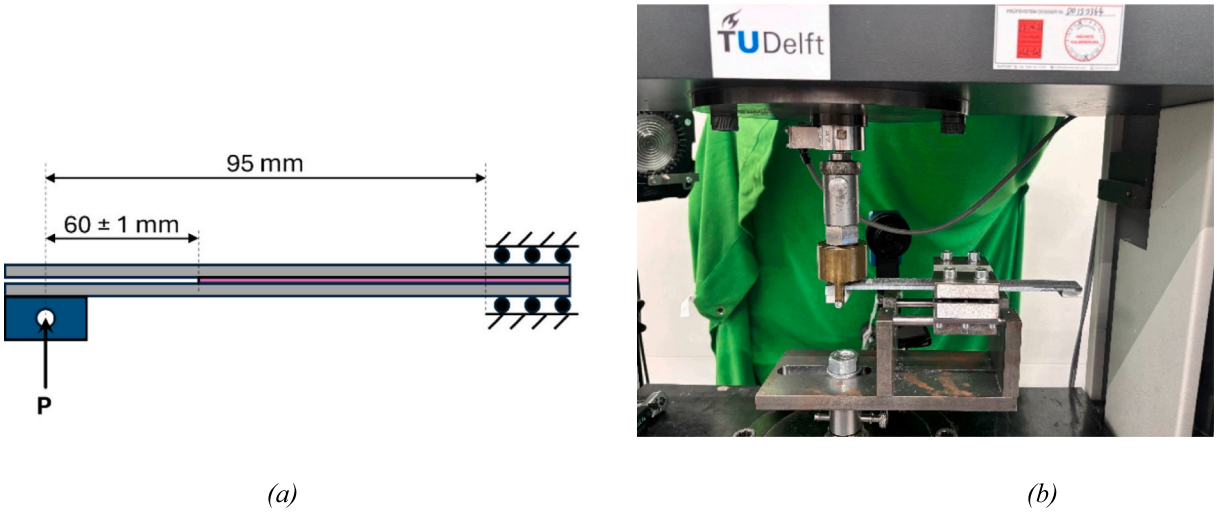

Fig. 4. (a) Schematic representation of CELS samples (figure not to scale), (b) testing of CELS specimens.

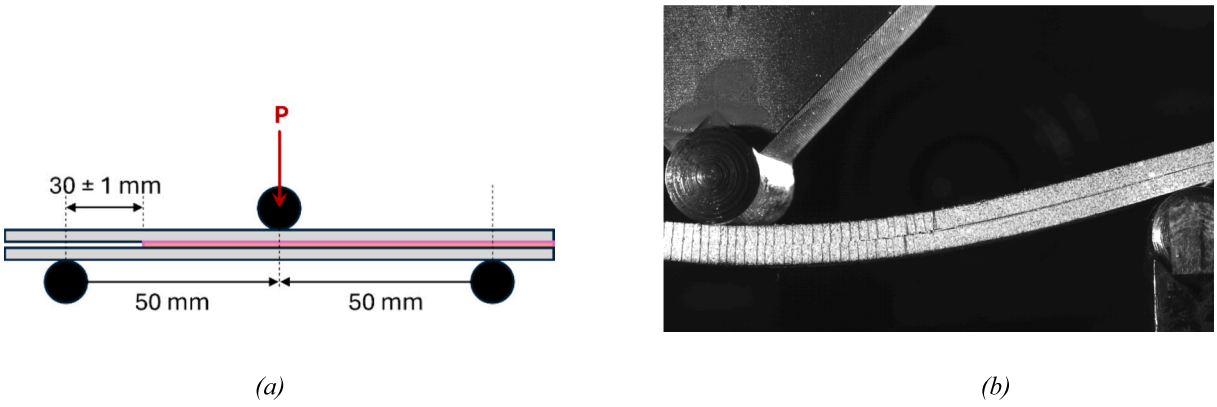

Fig. 5. (a) Schematic representation of ENF samples (figure not to scale), (b) shift of vertical marking demonstrating crack propagation.

was restricted to the 50:50 ratio. This approach is widely supported in the literature as a critical benchmark for determining the B–K power-law coefficient *(η)*, allowing for an accurate assessment of the failure envelope without unnecessary redundancy.

While compliance-based methods such as CBTE and CBBM are well-established for Mode II configurations (CELS and ENF) and are supported by standards such as ISO 15114 [42], a similarly standardized, universally accepted equivalent crack length method for the MMB test is currently lacking. To ensure the highest level of data integrity and reliability, this study strictly adhered to ASTM D6671 [63], which prescribes the visual crack-tracking method. The MMB test introduces significant complexities that are not present in simpler Mode II tests, including:

- Fixture Constraints: The significant weight of the MMB apparatus and the resulting gravitational forces must be precisely balanced.

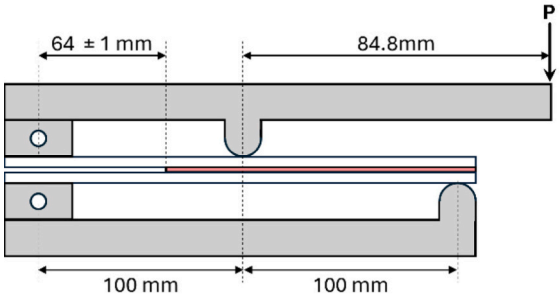

(a)

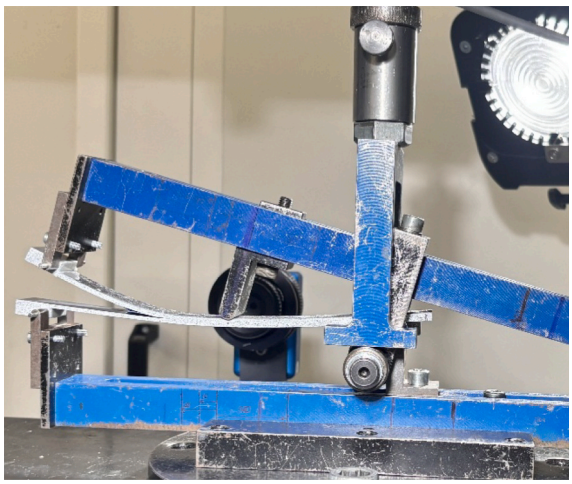

(b)

Fig. 6. (a) Schematic representation of MMB samples (figure not to scale), (b) crack opening and propagation showcasing mixed mode loading,

- Geometric Sensitivity: The accuracy of the results is highly dependent on the precise measurement of the lever arm length (c) and the constant monitoring of the loading mid-span.
- Mode Partitioning: Using the visual method in conjunction with the standard's analytical framework allowed us to address the limitations of classical mode partitioning without introducing the additional uncertainties inherent in non-standardized equivalent-crack-length methods for mixed-mode loading.

By strictly following the ASTM D6671 [63] standard and aligning with the existing body of literature on toughened aerospace adhesives, we ensured that our characterization of the fracture envelope remains benchmarked against validated protocols.

2.3.5. *Mixed mode: crack lap shear*

The Crack Lap Shear (CLS) test was employed to evaluate the mixed-mode fracture behavior of adhesively bonded joints, primarily governed by in-plane shear loading [40]. The CLS configuration was first introduced by Brussat et al. [64], in which two adherends of unequal span lengths are bonded together with an initial pre-crack (Fig. 7). During

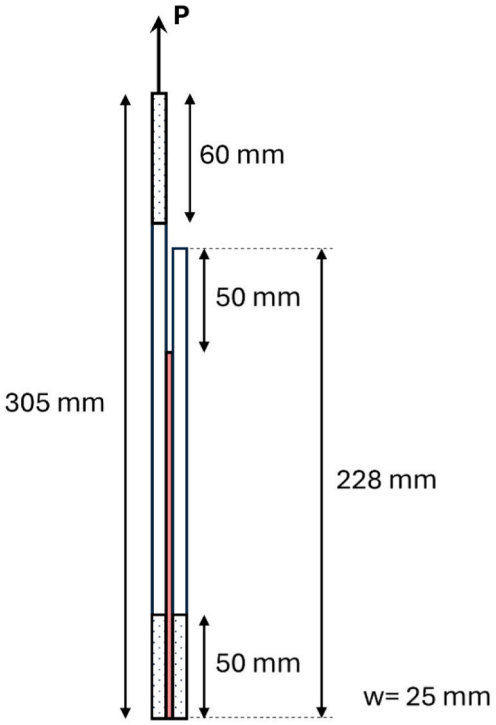

(a)

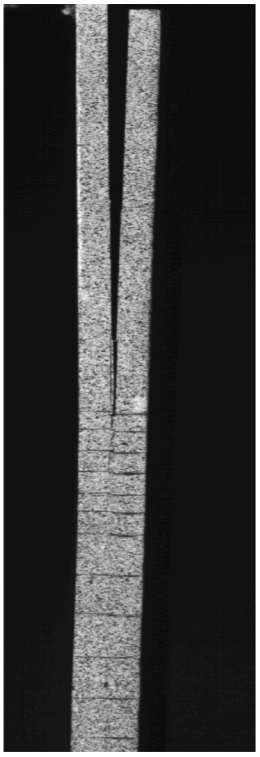

(b)

Fig. 7. (a) Schematic representation of CLS samples (figure not to scale). (b) Shift of vertical marking demonstrating crack propagation induced by peeling and shearing stress.

testing, the longer arm of the specimen is subjected to tensile loading, inducing a stable strain energy release rate under mixed-mode conditions. This behavior is strongly influenced by the higher bond-length-to-arm-thickness ratio of the specimen.

Tensile loading applied parallel to the adhesive bond line predominantly generates in-plane shear stresses, imparting a strong Mode II component. However, due to the inherent eccentricity in the loading direction, a secondary out-of-plane peeling stress is introduced, resulting in a Mode I contribution. The simultaneous presence of shear and peeling stresses results in mixed-mode loading conditions at the crack tip.

The length of the longer arm was kept at 305 mm, whereas the shorter arm measured 228 mm. The bonding length of 178 mm was maintained at a relatively large value to characterize a fully developed R-curve and achieve a higher bond length-to-arm thickness ratio for the specimen. The initial crack length a_0 was kept equal to 50 mm.

3. Results and discussions

3.1. DCB

All specimens demonstrated excellent repeatability, exhibiting stable crack propagation along the adhesive bond line with a cohesive failure mode. The average peak load recorded across all samples was 244.10 ± 1.45 N, with a standard deviation of 0.60%. The corresponding displacement at peak load was 19.11 ± 0.37 mm, reflecting a variation of 1.96%. The specimens displayed relatively high compliance due to the flexibility of the adherend, resulting in large displacements prior to complete separation (Fig. 8). A carrier bridging effect was observed as the crack propagated, induced by the woven knit carrier within the AF163-2K adhesive film. This carrier-bridging phenomenon (see Fig. 3b and c) served as an intrinsic toughening mechanism, promoting enhanced energy absorption during crack growth and resulting in a more tortuous crack path [25,73,74]. Consequently, the fracture resistance during crack propagation exceeded that at initiation, as reflected in the characteristic R-curve behavior. For Mode I (DCB), the Modified Beam Theory (MBT) was applied per ASTM D5528 [41]. The $G_{I_c}^{init}$ for the specimens was 3.05 ± 0.20 N/mm which was determined at the point of visual crack onset, while the G_{Ic}^{prop} was 3.48 ± 0.23 N/mm. This was extracted once the R-curve reached a stable rising trend. The R-curve exhibited a distinct plateau region, displaying stable crack growth and consistent toughening behavior resulting from carrier bridging, despite the high compliance of the DCB configuration. A similar extrinsic toughening mechanism has been previously reported for adhesive AF163-2K [25,75].

3.2. CELS

The force-displacement response for the pre-cracked CELS specimens is shown in Fig. 11a. All samples exhibited stable disbond growth characterized by cohesive failure within the adhesive layer. The average failure load was 934 ± 31.6 N, with minor variation in displacement among samples, confirming minimal deviation in the initial pre-crack length. The relatively high displacement observed across specimens is attributed to the lower overall thickness of the CELS configuration (Figs. 4 and 9a). Accordingly, a significant displacement correction factor (F) was applied in subsequent data reduction calculations, while the end-block correction factor (N) was found to be negligible and was therefore omitted [58,76].

A large FPZ ahead of the crack tip was observed in the CELS specimens, which complicates accurate crack tip tracking and energy release rate estimation [77]. The Corrected Beam Theory with Effective Crack Length (CBTE) method, as specified in ISO 15114 [42], was used to evaluate G_{IIC}. This method uses an effective crack length to account for compliance-related effects and the FPZ present in the toughened AF 163-2K adhesive. The Mode II critical fracture toughness G_{IIC} was extracted from the plateau value of the steady state region of the crack propagation before increased constraint from the clamp, and was 11.2 ± 0.93 N/mm. Mode II CELS tests generated a broader shear-driven FPZ, distributing damage ahead of the crack tip, effectively reducing the localized energy release rate and yielding a conservative estimate of fracture toughness (see Figs. 9c and 15b).

Fig. 9c illustrates the interaction between the FPZ and the resulting fracture toughness measurement in shear-dominant modes. The arrow indicates the evolutionary path of energy dissipation: as the FPZ matures and reaches a steady state, the system transitions from localized microcracking to G_{IIC} measurement. The length of the FPZ was experimentally determined using DIC, specifically by identifying the zone of non-linear strain (micro-cracking and plastic deformation) that precedes the actual crack tip.

3.3. 3-point-bending ENF

Mode II fracture characterization was further performed using the ENF test to assess the influence of compliance under in-plane shear-dominated loading. All ENF specimens exhibited stable crack propagation with a cohesive failure mode within the adhesive layer. The corresponding force-displacement response is presented in Fig. 10a. The tests demonstrated excellent repeatability, with an average maximum failure load of 3240 ± 134 N. The displacement at maximum load was notably lower than that observed in the CELS specimens, indicating a stiffer global response and reduced compliance effects due to the

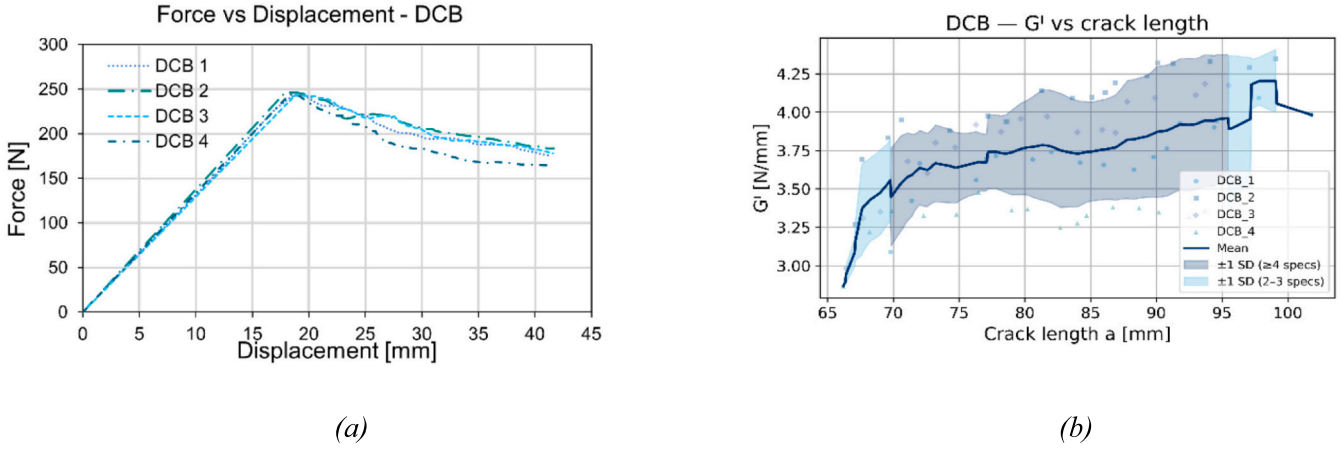

Fig. 8. (a) Experimental load-displacement curve for the DCB test, (b) Experimental R-curve for the DCB specimens using the MBT data reduction scheme.

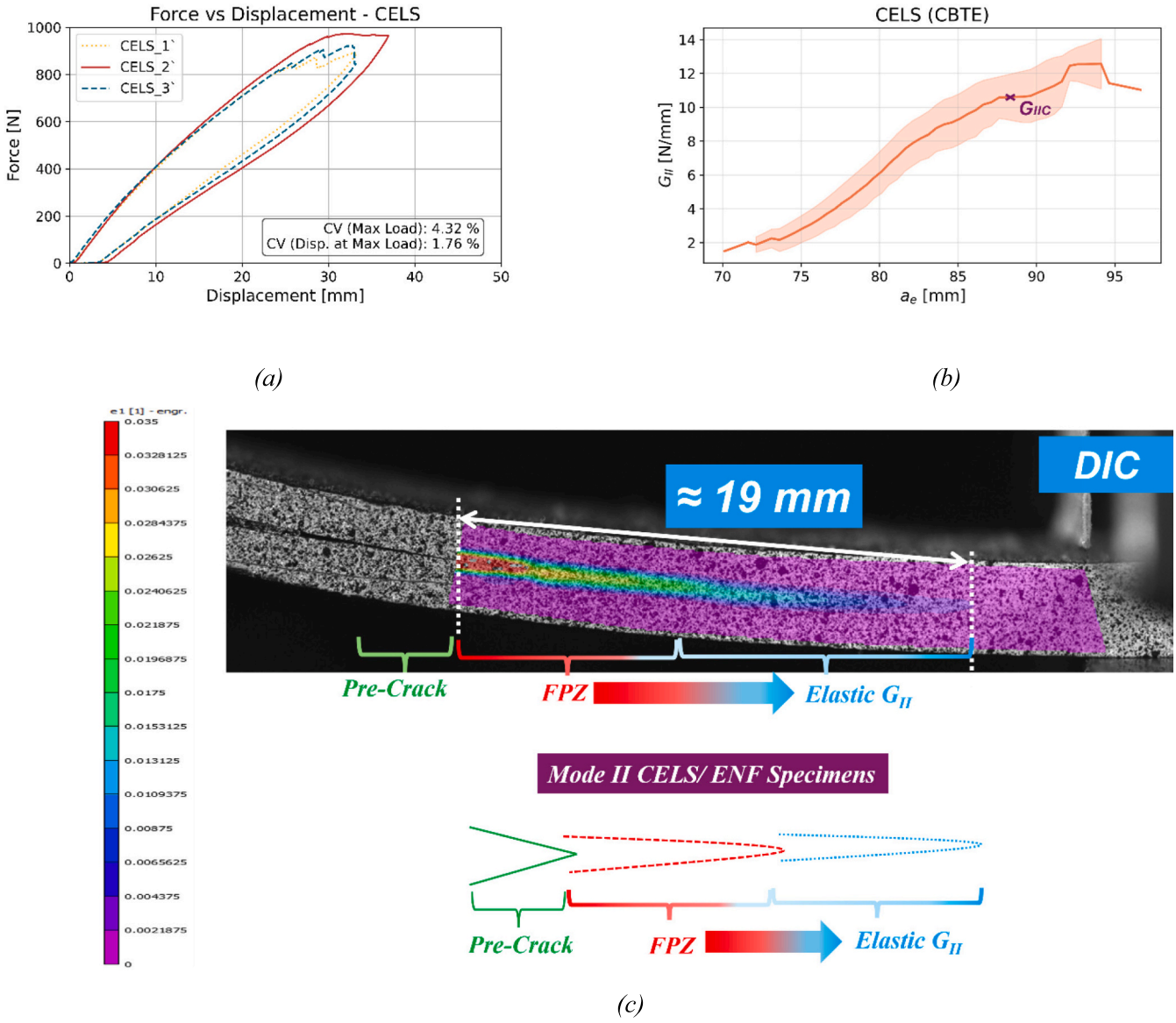

Fig. 9. (a) Experimental load-displacement curve for the CELS test, (b) experimental R-curve for the CELS specimens using the CBTE data reduction scheme, (c) broader shear-driven FPZ that distributes damage ahead of the pre-crack tip, thereby reducing the localized energy release rate at the crack tip and yielding a conservative fracture toughness estimate

symmetric three-point bending configuration.

The nonlinear region of the load-displacement curve revealed pronounced plastic deformation, associated with the development of a FPZ ahead of the crack tip [59]. This FPZ contributes to localized plasticity in the later stages of fracture (Fig. 15c).

The critical Mode II strain energy release rate (G_{IIC}) was evaluated at the peak force to avoid the parasitic effects of local compression and constraints imposed by the loading indenter, a standard protocol in the literature to ensure data integrity [52,60–62,78]. The average G_{IIC} value obtained using the CBBM method, following De Moura's methodology [57], was 11.85 ± 0.872 N/mm, which is close to the value measured for the CELS configuration (Fig. 10b). The resemblance in the G_{IIC} value using the CBBM method is due to its ability to isolate the change in compliance that dictates SERR.

3.4. MMB

Mixed-mode fracture characterization was conducted using the MMB configuration at a Mode I/Mode II ratio of 50:50, allowing for a power-criterion correlation with pure mode tests. The MMB specimens exhibited stable crack propagation accompanied by cohesive failure within the adhesive layer, consistent with the behavior observed in the DCB, CELS, and ENF tests. The average failure load was 597 ± 21.2 N, with the specimens displaying relatively large displacements due to their inherent compliance (Fig. 11a). Data reduction analyses revealed that the R-curve for the MMB test (Fig. 11b) exhibits an initial rising trend followed by a notable reduction in slope gradient as the crack extends. The transition from a continuous, steep increase in fracture resistance to an approaching steady-state condition suggests the gradual stabilization of energy dissipation mechanisms during crack growth. A similar rising effect of the R-curve was observed in Pure Mode II tests. The initial part of the R-curve is similar to that observed in the pure mode DCB test (Fig. 11b). The carrier bridging effect was also observed in the MMB test during crack propagation; however, it was much smaller than in the DCB test.

For Mixed-Mode (MMB) testing at a 50:50 ratio (ASTM D6671 [63]),

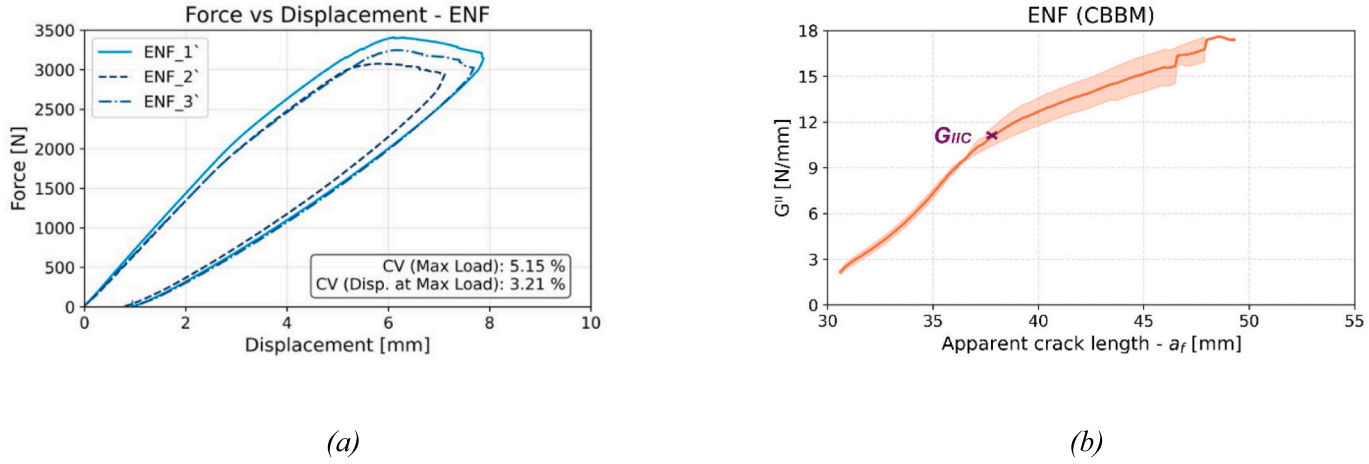

Fig. 10. (a) Experimental load-displacement curve for the ENF test, (b) Experimental R-curve for the ENF specimens using the CBTE data reduction scheme.

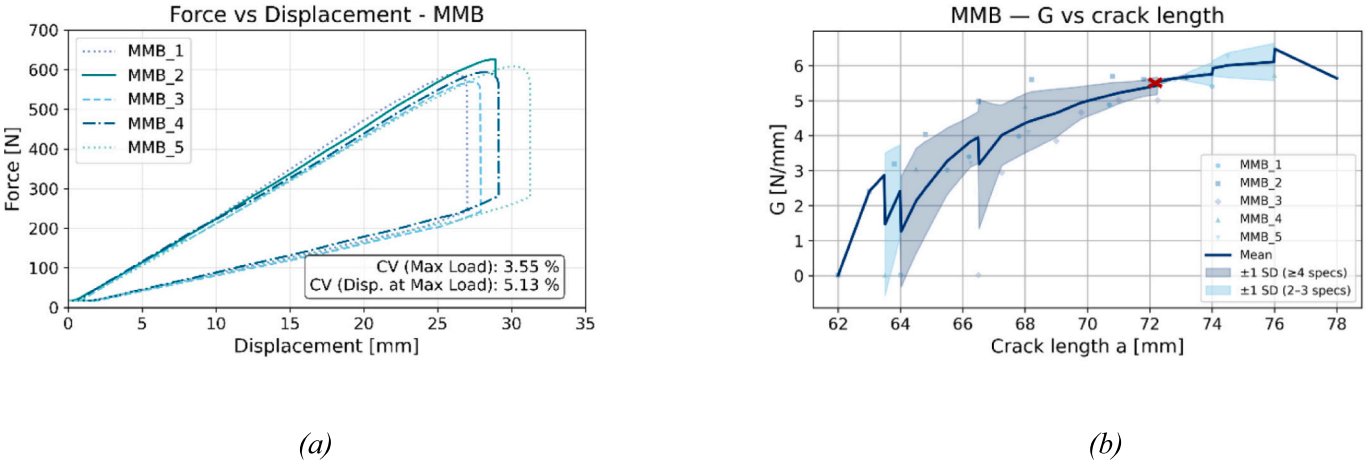

Fig. 11. (a) Experimental load-displacement curve for the MMB test. (b) Experimental R-curve for the MMB specimens.

the critical SERR was calculated at the non-linear (NL) point, representing the lower bound of fracture toughness. This was verified against visual initiation methods, showing excellent agreement. The mean mixed-mode critical SERR(G_T) was 5.65 ± 0.52 N/mm, with a constant average experimentally determined mode mixity (ψ) of 0.508, demonstrating excellent repeatability across the tested specimens. The Benzeggagh-Kenane (B–K) criterion was employed to define the softening power-criterion relationship between the mixed-mode and pure-mode critical strain energy release rates. The critical values of G_{IC} and G_{IIC} obtained from the DCB and Mode II tests (CELS and ENF) were used as input parameters. The resulting B–K power-criterion coefficient (η) was determined to be approximately 1.73. However, due to the difficulty

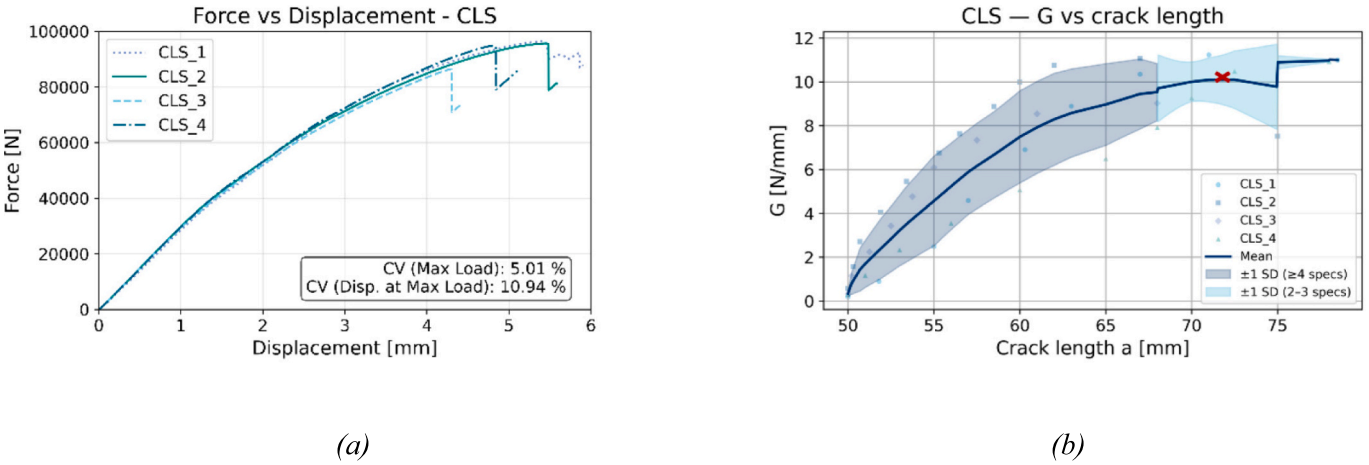

Fig. 12. (a) Experimental load-displacement curve for the CLS test, (b) experimental R-curve for the CLS specimens using Kinloch data reduction scheme.

and differences in observing the crack tip, the critical G_T according to the second observer was 4.83 ± 0.95 N/mm, and the B–K power criterion coefficient (η) = 2.64.

3.5. CLS

The CLS specimens were tested to evaluate the mixed-mode fracture behavior of the bonded joints. The extracted results were used to quantify the inherent mode mixity of this geometry. The CLS

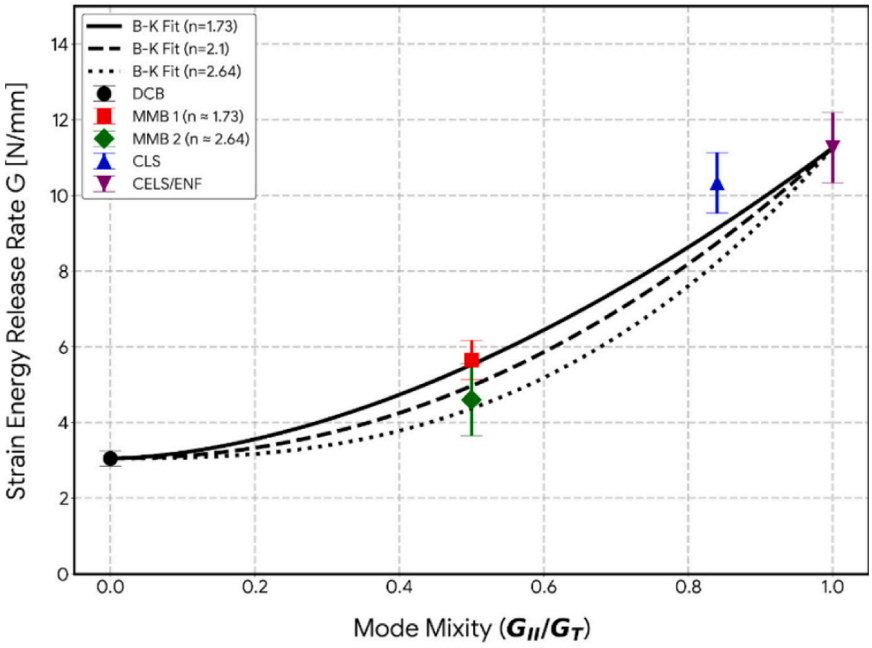

(a)

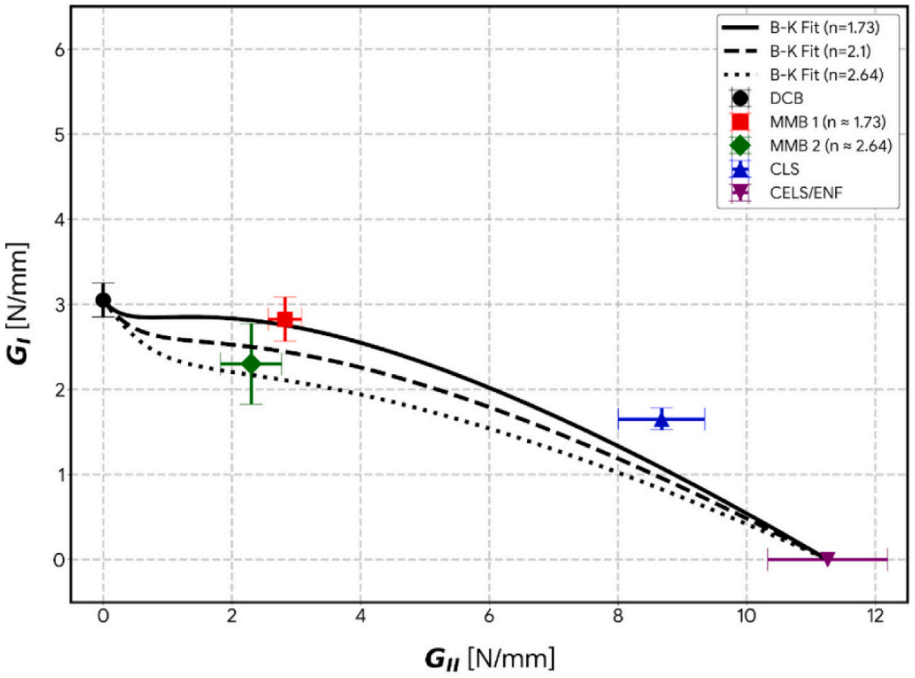

(b)

Fig. 13. (a) B–K power criterion fit from the pure modes and MMB tests vs. spline interpolation fit of critical SERR of pure mode test, MMB, and CLS test (MMB: First Observer, MMB 2: Second Observer). (b) The B–K power law deviation in the partition of individual mode fracture toughness compared with experimental partition (Kinloch), when the Mode II SERR is higher than the G_{mix}.

configuration exhibited significantly higher failure loads, with an average value of 93.4 ± 4.2 kN (Fig. 12). This elevated strength arises from the combined effect of the tensile resistance of the unidirectional IM7/8552 laminates and the high shear strength of the AF163-2K adhesive. All specimens displayed stable crack growth with cohesive failure within the adhesive layer, with no evidence of crack migration into the composite adherends.

The Kinloch data-reduction scheme [34,74] was employed to construct the R-curve and determine the mixed-mode strain energy release rate, G_{mix}. This data-reduction scheme is commonly used for ductile adhesives and provides an effective calculation of the individual mode contribution [37,40,79]. The R-curve exhibited a steady rise followed by a distinct plateau, indicating stable crack propagation. The mean G^c_{mix} for the CLS specimens at the plateau was 10.33 ± 1.03 N/mm, characterized by a global, effective mode mixity of $G_I/G_{II} \approx 0.20$, reflecting a strong Mode II dominance at the later stage of the fracture process (Figs. 12b and 13).

3.6. Curve fitting and mode-partitioning

A reverse analysis using the B–K relation with the exponent "$\eta = 1.73, 2.1, and\ 2.64$" was carried out using the results of the MMB test, in conjunction with the pure mode test, to get a complete B–K envelope having different mode mixity. Incorporating DCB, CELS/ENF, MMB, and CLS critical SERRs with their respective mode-mixities serves as a reference for understanding the limitations of different mixed-mode formulations, particularly under Mode II-dominant loading, where large fracture process zones are present. This reference was also found to be suitable, where the toughening mechanism creates distributed energy dissipation [33,37,80]. At maximum load, the mean Mode II component G_{II} was 8.77 ± 1.05 N/mm, while the corresponding Mode I component G_I was 1.68 ± 0.16 N/mm, clearly reflecting the combined influence of shear and peeling stresses. The geometric eccentricity between the longer and shorter arms of the CLS configuration introduces a small peeling component, but the large bond-length-to-thickness ratio ensures that most of the load is transferred through shear. Crack initiation occurred near the end of the Teflon insert, driven by localized peeling stresses after measurable bending of the shorter arm. As the loading progressed, shear stresses dominated the response, enhancing the failure resistance and resulting in higher mixed-mode fracture toughness.

However, when plotting the B–K power-criterion fit derived from the pure modes and the MMB test alongside the CLS test results, notable deviations of up to ≈20 to 30% emerged when the Mode II contribution increased, reaching a global, effective mode mixity of $G_I/G_{II} \approx 0.20$ (Fig. 13). This significant deviation persisted even after accounting for the large Mode II FPZ size using the CBTE or CBBM data reduction scheme for CELS or ENF. Furthermore, relying on classical Mode II data reduction schemes, such as CCM and CBT, which do not account for the larger FPZ or the compliance differences inherent in using varied test setups, would result in even greater discrepancies.

The observed discrepancies suggest that the B–K envelope's limitation to capture the failure process arises from a fundamental issue of LEFM-based mixed-mode partitioning in the presence of large, evolving FPZs. The G_{mix} value obtained from the Kinloch [79] approach relies on linear elastic assumptions and does not account for the extensive and evolving FPZ characteristic of Mode II-dominant loading in toughened adhesives. As the FPZ size and morphology in the CLS specimen differ significantly from the MMB calibration tests, the physical distribution of energy between the opening and shearing modes is altered. Consequently, applying a single empirical relationship leads to incorrect estimates of individual mode contributions, particularly when the Mode II component is large enough to shift the effective crack tip location beyond the limits of conventional data reduction, thereby limiting fracture toughness prediction.

3.7. FPZ analysis and computational studies

Experimental observations using DIC were correlated with computational modeling of the FPZ to gain a better understanding of how the FPZ governs mode-mixity. The computational analyses were performed using Abaqus/CAE 6.24 [81]. Two-dimensional plane-strain finite element (FE) models were developed to simulate the experimental configurations while maintaining computational efficiency [82,83]. While 3D Finite Element Analysis (FEA) was initially performed to validate the experimental results and the 2D assumptions, we found that the results between the 2D and 3D models were nearly identical. Given the high computational cost of 3D modeling, even with high-performance computing resources, the 2D plane-strain model was selected for the final parametric studies. This choice allowed for significantly higher mesh refinement within the adhesive layer without compromising the accuracy of the structural response. Each adherend was discretized into 16 individual plies, consistent with the experimental laminate stacking sequence. A thin delamination layer was introduced just above the first ply adjacent to the adhesive interface to monitor potential secondary crack initiation and migration (Fig. 14).

The material properties of unidirectional (UD 0^0) IM7/8552 and the interlaminar resin were obtained from the literature [84,85]. Each ply was assigned the appropriate material orientation along the fiber direction. The elastic and fracture properties used in the numerical models are summarized in Tables 1 and 2. The adhesive film (AF163-2K) was represented using a cohesive interface layer tied to the upper and lower adherends through a surface-based tie constraint. A bilinear cohesive traction–separation law was adopted to simulate the behavior of both the adhesive disbond and delamination layers [86,87]. The quadratic stress criterion (QUADS) was used to define the adhesive's damage-initiation traction behavior. A single layer of cohesive elements was employed through the adhesive thickness to capture its response. A mesh convergence study was conducted along the length to assess numerical accuracy and ensure mesh independence. A consistent global element size of 0.1 mm was applied throughout the model.

The mode I critical strain energy release rate (G_{IC}) of the adhesive was obtained from the DCB tests. The mode II value (G_{IIC}) was derived from post-processing of the CELS and ENF specimens. The B–K power criterion [88] was used to describe the mixed-mode fracture criterion, with the exponent value calibrated from MMB tests (Table 3). Since the experimental fracture energies in this study aligned closely with established data for AF 163-2K in the following literature [44,45], the interfacial strengths were adopted from validated literature sources to define the peak of the traction-separation law. The geometry and boundary conditions applied in the numerical models accurately replicated the experimental setup.

The numerical simulations consistently reproduced stable cohesive failure within the adhesive layer, in agreement with the experimental failure mode. The scalar stiffness degradation (SDEG) contour plots obtained from the simulations further substantiated these findings, demonstrating a progressive damage evolution pattern consistent with cohesive failure mechanisms observed experimentally (see Fig. 15). The numerical results, with excellent fidelity, accurately captured the softening behavior that occurs after propagation. Furthermore, the plastic softening region in the simulated curves showed a close resemblance to the experimental results, highlighting an identical FPZ.

Pure Mode I (DCB) simulations, correlated with DIC, revealed a small, localized FPZ ahead of the crack tip, characterized by minor plastic deformation. The observed carrier bridging, a toughening mechanism that occurs behind the crack tip and significantly enhances propagation toughness, indirectly influences the formation of the FPZ. In contrast, analysis of the pure Mode II (CELS and ENF) tests revealed that the FPZ formed substantially ahead of the crack tip, resulting in a large apparent toughness and the characteristic rising R-curve behavior. This necessitated the use of methods like CBTE for accurate characterization, as it explicitly accounts for the large apparent crack length associated

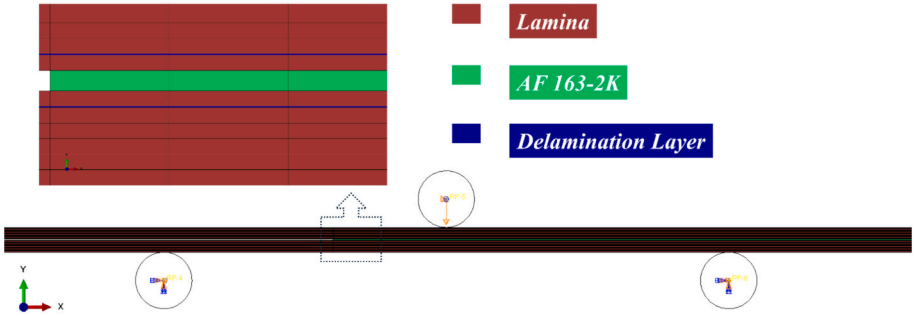

Fig. 14. Schematic representation of ENF specimen (similar for other configurations) modeled in Abaqus CAE 6.24.

Table 1
Material properties of IM7/8552 [84,85].

E_{11} [MPa]	146,700
$E_{22} = E_{33}$ [MPa]	8700
$G_{12} = G_{13}$ [MPa]	5160
G_{23} [MPa]	3000
$\upsilon_{12} = \upsilon_{13}$	0.3
υ_{23}	0.4

Table 2
Cohesive element properties for IM7/8552 used in FE modeling [85].

G_{IC} [N/mm]	G_{IIC} [N/mm]	σ_n [MPa]	σ_t [MPa]
0.24	0.739	80.1	97.6

Table 3
Final cohesive properties to be used in FE modeling.

G_{IC} [N/mm]	G_{IIC} [N/mm]	σ_n [MPa]	σ_t [MPa]	η
3.05	11.2	35	35	1.73

with the extended FPZ.

In the MMB test, the FPZ size was larger than DCB but notably smaller than CELS/ENF. Crucially, the FPZ size was observed to be constant throughout the propagation phase, as the mode-mixity was not evolving. The standard MMB data reduction scheme attempts to incorporate the FPZ contribution; however, it implicitly accounts for the influence of FPZ size and compliance effects by incorporating correction factors primarily derived from pure Mode I tests, such as the DCB test. This approach implicitly assumes that FPZ characteristics remain comparable across different mode-mixities. It forces a peeling-dominated Mode I-centric correction and underestimates the large and diffused shear-dominated contribution by Mode II. Hence, it is likely masking the true, mode-dependent FPZ behavior in the mixed-mode measurement.

Conversely, the CLS test exhibited a constantly evolving FPZ driven by the initial elastic bending to stabilized plastic shear deformation influencing the mode mixity. The increasing Mode II contribution led to the FPZ continuously increasing in size as the test progressed, transforming into a region of large, evolving plastic deformation, similar to that observed in the CELS/ENF tests.

The B–K power criterion fit (derived from MMB and pure mode data) is compared against the SERR of CLS specimens; notable deviations emerge as the individual mode II component becomes dominant. This underestimation of the MMB-derived B–K curve in accurately predicting the apparent fracture toughness of the CLS specimens highlights its limitations when applied to complex mixed-mode tests with a mode-dependent, evolving FPZ. Hence, this highlights the need for FPZ-sensitive data-reduction methods to be employed in complex mixed-mode situations. This will enable a more physical representative comparison of mixed-mode fracture toughness across different test configurations.

4. Conclusions

This study provides a comprehensive analysis of the evolution of the Fracture Process Zone (FPZ) in adhesively bonded CFRP joints across five distinct configurations (DCB, CELS, ENF, MMB, and CLS). By correlating carrier bridging, compliance, and mode-mixity, a clear distinction emerges between standardized characterization and structural-level validation.

While standardized tests like DCB, ENF, and MMB establish the foundational fracture envelope used in aerospace certification, this research demonstrates that structural-level joints—exemplified here by the CLS specimen—exhibit complex behaviors that deviate from these idealized predictions. Specifically, the Benzeggagh–Kenane (B–K) criterion derived from coupon-level MMB tests conservatively underestimated the CLS fracture response by 20%–30%. This discrepancy highlights that fracture parameters are not always directly transferable when the loading environment transitions from stable, self-similar growth to configurations with evolving mode-mixity.

- FPZ is highly mode-dependent, and its evolution mechanism plays a governing role in crack growth and R-curve behavior.
- The significant ≈20%–30% deviation between the MMB-derived B–K prediction and the CLS specimen data clearly indicated that the FPZ evolution is configuration and mode-dependent. This deviation in accurately predicting SERR in mixed-mode joints remained even after accounting for the large Mode II FPZ size using CBTE or CBBM. Hence, the B–K criterion, derived from a single standard test like MMB (which has a stable, constant FPZ), is not reliably transferable to complex, structurally relevant loading conditions, such as the CLS test.
- The CLS configuration represents a structural-type joint, where geometric effects, large FPZ development, and evolving mode mixity influence the global response. Consequently, the CLS test should be interpreted as a structural validation case rather than a strict fracture characterization method. In this study, the mode mixity ($G_I/G_{II} \approx 0.20$) was therefore evaluated only at the critical point corresponding to crack initiation.
- The comparison between CLS results and the fracture envelope highlights that fracture parameters derived from idealized coupon-level tests may conservatively underestimate the response of larger structural joints, emphasizing the importance of validating fracture characterization results in structurally representative configurations.
- Standard data reduction schemes (e.g., in MMB, relying on Mode I corrections) are inadequate because they mask the true, mode-dependent FPZ behavior. Accurate fracture characterization for toughened adhesives requires FPZ-sensitive methods (like CBTE or CBBM for G_{IIC} and correlation with DIC/CZM) to capture the actual material deformation.

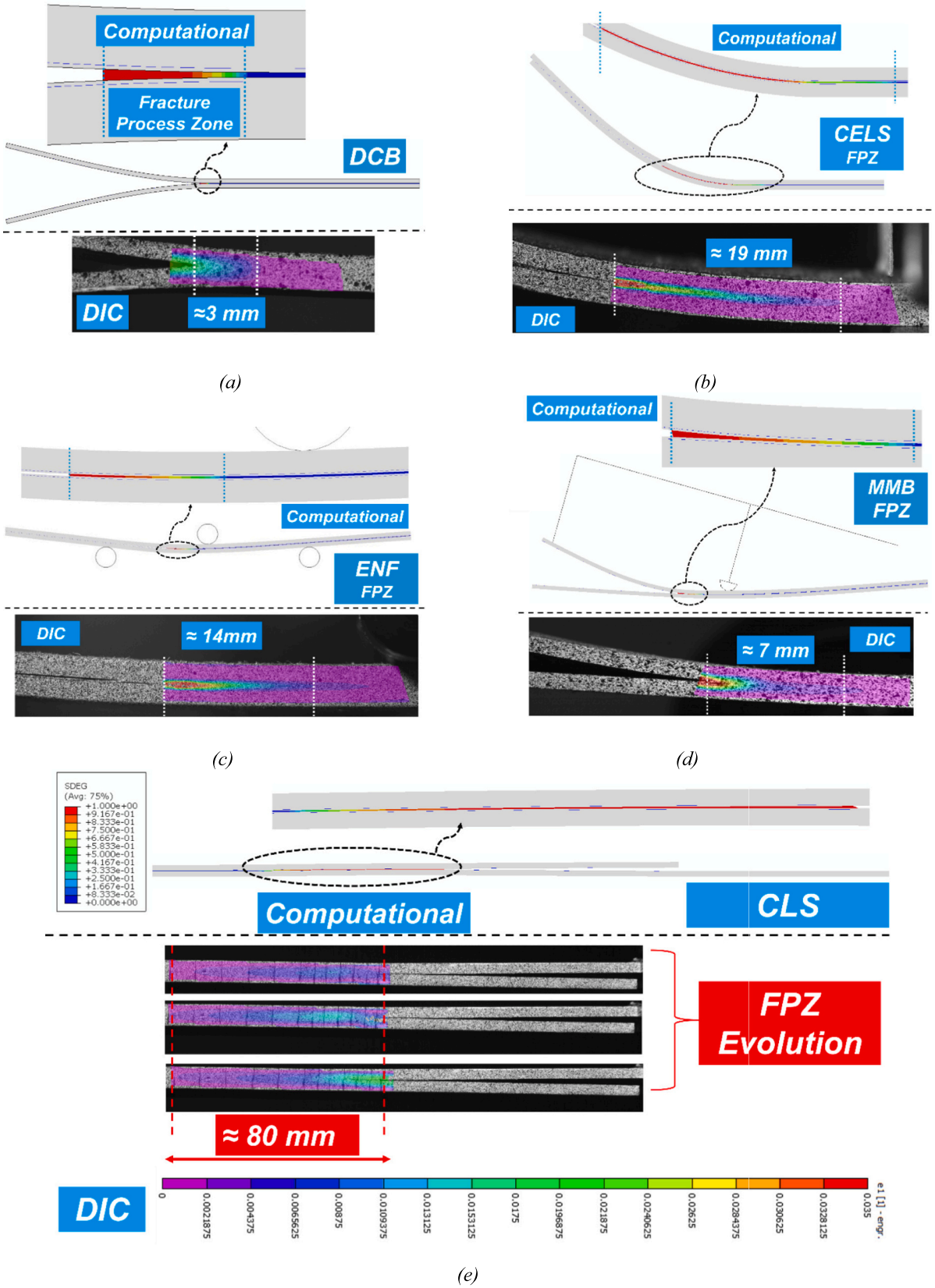

Fig. 15. Comparison of the evolution of the FPZ from computational models with DIC (for legend see (e)) (a) DCB; Very small, localized FPZ (b) CELS; Large FPZ ahead of the crack tip (c) ENF; Large FPZ ahead of the crack tip; less than CELS due to smaller compliance (d) MMB; Moderate FPZ (e) CLS; Size of FPZ is evolving as the mode II contribution is increasing.

While FPZ-sensitive methods are available for analyzing the standard pure mode II tests (e.g., CBTE or CBBM), further work is needed to understand how to correctly incorporate the effect of FPZ size into the analysis of more complex mixed-mode configurations.

CRediT authorship contribution statement

Ishan Manoj: Writing – original draft, Visualization, Validation, Methodology, Investigation, Formal analysis, Data curation, Conceptualization. **Daniel Bernardes de Castro:** Writing – review & editing, Visualization, Validation, Investigation, Formal analysis, Data curation. **John-Alan Pascoe:** Writing – review & editing, Visualization, Supervision, Resources, Methodology, Funding acquisition, Conceptualization. **René Alderliesten:** Writing – review & editing, Visualization, Supervision, Resources, Methodology, Funding acquisition, Conceptualization.

Declaration of competing interest

The authors declare that they have no known competing financial interests or personal relationships that could have appeared to influence the work reported in this paper.

Acknowledgement

The project was carried out with a subsidy from the TSH Aircraft Manufacturing scheme of the Ministry of Economic Affairs, implemented by the Netherlands Enterprise Agency (RVO).

Appendix A. Supplementary data

Supplementary data to this article can be found online at https://doi.org/10.1016/j.tafmec.2026.105617.

Data availability

Data will be made available on request.

References

[1] S. Budhe, M.D. Banea, S. de Barros, L.F.M. da Silva, An updated review of adhesively bonded joints in composite materials, Int. J. Adhes. Adhes. 72 (2017) 30–42, https://doi.org/10.1016/j.ijadhadh.2016.10.010.
[2] N.K. Akkasali, S. Biswas, S. Sen, S. Anitha, A state-of-the-art review on adhesively bonded joints of similar and dissimilar materials, J. Adhes. Sci. Technol. 38 (2024) 4317–4371, https://doi.org/10.1080/01694243.2024.2384421.
[3] J.A. Pascoe, R.C. Alderliesten, R. Benedictus, Methods for the prediction of fatigue delamination growth in composites and adhesive bonds - a critical review, Eng. Fract. Mech. 112–113 (2013) 72–96, https://doi.org/10.1016/j.engfracmech.2013.10.003.
[4] G. Jeevi, S.K. Nayak, Kader M. Abdul, Review on adhesive joints and their application in hybrid composite structures, J. Adhes. Sci. Technol. 33 (2019) 1497–1520, https://doi.org/10.1080/01694243.2018.1543528.
[5] J.A. Pascoe, Fracture and failure of adhesives, in: Comprehensive Structural Integrity, Elsevier, 2023, pp. V7-2–V7-23, https://doi.org/10.1016/B978-0-12-822944-6.00042-6.
[6] S. Ebrahimi, B. Behjat, M. Kouhi, The effect of loading rate on mixed mode I/II fracture behavior of adhesively bonded joints: experimental and numerical approach, Theor. Appl. Fract. Mech. 131 (2024), https://doi.org/10.1016/j.tafmec.2024.104420.
[7] S. Akpinar, R. Sahin, The fracture load analysis of different material thickness in adhesively bonded joints subjected to fully reversed bending fatigue load, Theor. Appl. Fract. Mech. 114 (2021), https://doi.org/10.1016/j.tafmec.2021.102984.
[8] I. Manoj, S. Kumar, A. Jain, A numerical study on stress mitigation in through-thickness tailored bi-adhesive single-lap joints, J. Adhes. Sci. Technol. 37 (2023) 3652–3686, https://doi.org/10.1080/01694243.2023.2217674.
[9] A.Y. Kanani, X. Hou, J. Ye, The influence of notching and mixed-adhesives at the bonding area on the strength and stress distribution of dissimilar single-lap joints, Compos. Struct. 241 (2020) 112136, https://doi.org/10.1016/j.compstruct.2020.112136.
[10] C. Sarrado, A. Turon, J. Costa, J. Renart, On the validity of linear elastic fracture mechanics methods to measure the fracture toughness of adhesive joints, Int. J. Solids Struct. 81 (2016) 110–116, https://doi.org/10.1016/j.ijsolstr.2015.11.016.
[11] A. Ameli, M. Papini, J.A. Schroeder, J.K. Spelt, Fracture r-curve characterization of toughened epoxy adhesives, Eng. Fract. Mech. 77 (2010) 521–534, https://doi.org/10.1016/j.engfracmech.2009.10.009.
[12] S. Askarinejad, E. Martínez-Pañeda, I.I. Cuesta, N. Fleck, Mode II fracture of an MMA adhesive layer: theory versus experiment, Eur. J. Mech. A Solids 86 (2021), https://doi.org/10.1016/j.euromechsol.2020.104133.
[13] I.S. Floros, K.I. Tserpes, T. Löbel, Mode-I, mode-II and mixed-mode I+II fracture behavior of composite bonded joints: experimental characterization and numerical simulation, Compos. Part B Eng. 78 (2015) 459–468, https://doi.org/10.1016/j.compositesb.2015.04.006.
[14] S. Kumar, B.L. Wardle, M.F. Arif, Strength and performance enhancement of bonded joints by spatial tailoring of adhesive compliance via 3D printing, ACS Appl. Mater. Interfaces 9 (2017) 884–891, https://doi.org/10.1021/acsami.6b13038.
[15] M.A. Khan, S. Kumar, J.N. Reddy, Material-tailored adhesively bonded multilayers: a theoretical analysis, Int. J. Mech. Sci. 148 (2018) 246–262, https://doi.org/10.1016/j.ijmecsci.2018.08.017.
[16] S. Kumar, B.L. Wardle, M.F. Arif, J. Ubaid, Stress reduction of 3D printed compliance-tailored multilayers, Adv. Eng. Mater. 20 (2018), https://doi.org/10.1002/adem.201700883.
[17] J. Karami, D.G. Aggelis, A.S. Kojouri, J. Chevalier, D. Hemelrijck, K. A. Kalteremidou, An experimental study on the delamination fracture of a unidirectional thermoplastic composite under different in-plane loading modes using acoustic emission, Compos. Struct. 369 (2025), https://doi.org/10.1016/j.compstruct.2025.119333.
[18] P. Davies, G.D. Sims, B.R.K. Blackman, A.J. Brunner, K. Kageyama, M. Hojo, et al., Comparison of test configurations for determination of mode II interlaminar fracture toughness results from international collaborative test programme, Plastics Rubber Compos. 28 (1999) 432–437, https://doi.org/10.1179/146580199101540600.
[19] F.J.P. Chaves, L.F.M. Da Silva, M.F.S.F. De Moura, D.A. Dillard, V.H.C. Esteves, Fracture mechanics tests in adhesively bonded joints: a literature review, J. Adhes. 90 (2014) 955–992, https://doi.org/10.1080/00218464.2013.859075.
[20] B. Blackman, F. Sun, S. Teixeira de Freitas, S. de Barros, M. Moreira Arouche, A. Ivankovic, Understanding fracture mode-mixity and its effects on bond performance, in: Advances in Structural Adhesive Bonding, Second Edition, Elsevier, 2023, pp. 579–613, https://doi.org/10.1016/B978-0-323-91214-3.00015-6.
[21] W. Wang, S.T. De Freitas, J.A. Poulis, D. Zarouchas, A review of experimental and theoretical fracture characterization of bi-material bonded joints, Compos. Part B Eng. 206 (2021), https://doi.org/10.1016/j.compositesb.2020.108537.
[22] M.F.S.F. de Moura, P.M.L.C. Cavaleiro, F.G.A. Silva, N. Dourado, Mixed-mode I+II fracture characterization of a hybrid carbon-epoxy/cork laminate using the single-leg bending test, Compos. Sci. Technol. 141 (2017) 24–31, https://doi.org/10.1016/j.compscitech.2017.01.001.
[23] A. Arrese, F. Mujika, J. Renart, C. Sarrado, Adhesive bond characterization under mixed-mode i + II loading using the mmb test, Eng. Fract. Mech. 318 (2025), https://doi.org/10.1016/j.engfracmech.2025.110962.
[24] I. Manoj, A. Jain, International journal of adhesion and adhesives strength improvement and failure analysis of dissimilar FDM printed single-lap joints with tailored interface geometry, Int. J. Adhes. Adhes. 136 (2025) 103876, https://doi.org/10.1016/j.ijadhadh.2024.103876.
[25] R.A.A. Lima, R. Tao, A. Bernasconi, M. Carboni, N. Carrere, S. Teixeira de Freitas, Uncovering the toughening mechanisms of bonded joints through tailored CFRP layup, Compos. Part B Eng. 263 (2023), https://doi.org/10.1016/j.compositesb.2023.110853.
[26] M. Conroy, A.J. Kinloch, J.G. Williams, A. Ivankovic, Mixed mode partitioning of beam-like geometries: a damage dependent solution, Eng. Fract. Mech. 149 (2015) 351–367, https://doi.org/10.1016/j.engfracmech.2015.06.061.
[27] R.D.F. Moreira, M.F.S.F. de Moura, F.G.A. Silva, A novel strategy to obtain the fracture envelope under mixed-mode I+II loading of composite bonded joints, Eng. Fract. Mech. 232 (2020), https://doi.org/10.1016/j.engfracmech.2020.107032.
[28] D.R. Moore, A. Pavan, J.G. Williams, Fracture mechanics testing methods for polymers, adhesives and composites, Eur. Struct. Integrity Soc. 28 (2001) 3–375.
[journal] D. Quan, D. Yue, Y. Ma, G. Zhao, R. Alderliesten, On the mix-mode fracture of carbon fibre/epoxy composites interleaved with various thermoplastic veils, Compos. Commun. 33 (2022), https://doi.org/10.1016/j.coco.2022.101230.
[30] M.T. Ebrahimi, Z. Khaji, M. Fakoor, On mixed-mode fracture of brittle orthotropic solids: a novel micromechanical damage model, Eng. Fract. Mech. 313 (2025), https://doi.org/10.1016/j.engfracmech.2024.110628.
[31] A. Raimondo, I. Urcelay Oca, C. Bisagni, Influence of interface ply orientation on delamination growth in composite laminates, J. Compos. Mater. 55 (2021) 3955–3972, https://doi.org/10.1177/00219983211031636.
[32] L. Amaral, R. Alderliesten, R. Benedictus, Understanding mixed-mode cyclic fatigue delamination growth in unidirectional composites: an experimental approach, Eng. Fract. Mech. 180 (2017) 161–178, https://doi.org/10.1016/j.engfracmech.2017.05.049.
[33] D. Álvarez, F.J. Guild, A.J. Kinloch, B.R.K. Blackman, Partitioning of mixed-mode fracture in adhesively-bonded joints: experimental studies, Eng. Fract. Mech. 203 (2018) 224–239, https://doi.org/10.1016/j.engfracmech.2018.04.032.
[34] K. Shimamoto, Y. Sekiguchi, C. Sato, Mixed mode fracture toughness of adhesively bonded joints with residual stress, Int. J. Solids Struct. 102–103 (2016) 120–126, https://doi.org/10.1016/j.ijsolstr.2016.10.011.
[35] Y. Kouno, M. Imanaka, R. Hino, M. Omiya, F. Yoshida, R-curve behavior of adhesively bonded composite joints with highly toughened epoxy adhesive under

mixed mode conditions, Int. J. Adhes. Adhes. 105 (2021), https://doi.org/10.1016/j.ijadhadh.2020.102762.
[36] Tong L, Luo Q. Analysis of Cracked Lap Shear (CLS) Joints. n.d.
[37] R.B.P. Barros, R.D.S.G. Campilho, I.J. Sánchez-Arce, J.M.M. Dionísio, K. Madani, Evaluation of the cracked lap shear test for mixed-mode fracture toughness estimation of adhesive joints, Proc. Inst. Mech. Eng. L J. Mater. Des. Appl. 237 (2023) 2537–2550, https://doi.org/10.1177/14644207221140296.
[38] J. Jokinen, M. Kanerva, Analysis of cracked lap shear testing of tungsten-CFRP hybrid laminates, Eng. Fract. Mech. 175 (2017) 184–200, https://doi.org/10.1016/j.engfracmech.2017.01.029.
[39] G. Fernlund, J.K. Spelt, Mixed-mode Fracture Adhesive Characterization of Joints 50, 1994.
[40] R.B.P. Barros, R.D.S.G. Campilho, I.J. Sanchez-Arce, J.M.M. Dionisio, K. Madani, Experimental analysis on the mixed-mode fracture behavior of structural adhesives, Proc. Struct. Integrity 51 (2023) 17–23, https://doi.org/10.1016/j.prostr.2023.10.061. Elsevier B.V.
[41] Test Method for Mode I Interlaminar Fracture Toughness of Unidirectional Fiber-Reinforced Polymer Matrix Composites 2021. doi: https://doi.org/10.1520/D5528_D5528M-21.
[42] Fibre-reinforced plastic composites — Determination of the mode II fracture resistance for unidirectionally reinforced materials using the calibrated end-loaded split (C-ELS) test and an effective crack length approach ISI 15114. COPYRIGHT PROTECTED DOCUMENT. 2014.
[43] Test Method for Determination of the Mode II Interlaminar Fracture Toughness of Unidirectional Fiber-Reinforced Polymer Matrix Composites 2014. doi:https://doi.org/10.1520/D7905_D7905M-14.
[44] F. Sun, M. Lißner, N. Petrinic, B.R.K. Blackman, Universal slope-based j-integral methods for characterization of the mode i, mode II and mixed mode I/II fracture behaviour of adhesively bonded interfaces, Compos. Sci. Technol. 252 (2024), https://doi.org/10.1016/j.compscitech.2024.110611.
[45] F. Sun, Q. Wang, B.R.K. Blackman, Validity of LEFM to measure the mode II and mixed mode I/II fracture toughness of adhesively bonded CFRP, Compos. Part A Appl. Sci. Manuf. 192 (2025), https://doi.org/10.1016/j.compositesa.2025.108777.
[46] M. Demiral, F. Kadioglu, Failure behaviour of the adhesive layer and angle ply composite adherends in single lap joints: a numerical study, Int. J. Adhes. Adhes. 87 (2018) 181–190, https://doi.org/10.1016/j.ijadhadh.2018.10.010.
[47] F. Kadioglu, M. Demiral, Failure behaviour of the single lap joints of angle-plied composites under three point bending tests, J. Adhes. Sci. Technol. 34 (2020) 531–548, https://doi.org/10.1080/01694243.2019.1674101.
[48] D. Quan, G. Wang, G. Zhao, R. Alderliesten, On the fracture behaviour of aerospace-grade polyether-ether-ketone composite-to-aluminium adhesive joints, Compos. Commun. 30 (2022), https://doi.org/10.1016/j.coco.2022.101098.
[49] R.J.C. Carbas, E.A.S. Marques, L.F.M. da Silva, The influence of epoxy adhesive toughness on the strength of hybrid laminate adhesive joints, Appl. Adhes. Sci. 9 (2021), https://doi.org/10.1186/s40563-020-00132-5.
[50] M.A. Morgado, R.J.C. Carbas, D.G. Santos, L.F.M. da Silva, Strength of CFRP joints reinforced with adhesive layers, Int. J. Adhes. Adhes. 97 (2020), https://doi.org/10.1016/j.ijadhadh.2019.102475.
[51] F. Ramezani, P.D.P. Nunes, R.J.C. Carbas, E.A.S. Marques, L.F.M. da Silva, The joint strength of hybrid composite joints reinforced with different laminates materials, J. Adv. Joining Processes 5 (2022), https://doi.org/10.1016/j.jajp.2022.100103.
[52] M. Pérez-Galmés, J. Renart, C. Sarrado, A.J. Brunner, A. Rodríguez-Bellido, Towards a consensus on mode II adhesive fracture testing: experimental study, Theor. Appl. Fract. Mech. 98 (2018) 210–219, https://doi.org/10.1016/j.tafmec.2018.09.014.
[53] M.F.S.F. de Moura, R.D.S.G. Campilho, J.P.M. Gonçalves, Pure mode II fracture characterization of composite bonded joints, Int. J. Solids Struct. 46 (2009) 1589–1595, https://doi.org/10.1016/j.ijsolstr.2008.12.001.
[54] M. Mehrabi, L.M. Martulli, A. Bernasconi, M. Carboni, Estimating crack tip position in adhesively bonded joints subjected to mode II quasi-static loading, Fatigue Fract. Eng. Mater. Struct. 47 (2024) 1262–1280, https://doi.org/10.1111/ffe.14237.
[55] Y. Wang, J.G. Williams, Corrections for mode II fracture toughness specimens of composites materials, Compos. Sci. Technol. 43 (1992).
[56] M.F.S.F. de Moura, M.A.L. Silva, A.B. de Morais, J.J.L. Morais, Equivalent crack based mode II fracture characterization of wood, Eng. Fract. Mech. 73 (2006) 978–993, https://doi.org/10.1016/j.engfracmech.2006.01.004.
[57] M.F.S.F. de Moura, A.B. de Morais, Equivalent crack based analyses of ENF and ELS tests, Eng. Fract. Mech. 75 (2008) 2584–2596, https://doi.org/10.1016/j.engfracmech.2007.03.005.
[58] B.R.K. Blackman, A.J. Kinloch, M. Paraschi, The determination of the mode II adhesive fracture resistance, GIIC, of structural adhesive joints: an effective crack length approach, Eng. Fract. Mech. 72 (2005) 877–897, https://doi.org/10.1016/j.engfracmech.2004.08.007.
[59] J.P. Reis, M.F.S.F. de Moura, R.D.F. Moreira, Extension of the crack equivalent method applied to mode II fracture of thermoplastic composites bonded joints using the ENF test, Compos. Struct. 352 (2025), https://doi.org/10.1016/j.compstruct.2024.118687.
[60] M. Salamat-Talab, H. Kazemi, M. Mahdavi, Influence of yarn bundle orientation and areal density on the interlaminar fracture toughness of ENF composites, Eng. Fract. Mech. 315 (2025), https://doi.org/10.1016/j.engfracmech.2025.110806.
[61] M.M. Arouche, M. Pavlovic, Experimental and numerical analysis of the effect of temperature on the mode i and mode II delamination of glass fiber woven composites, Compos. Part B Eng. 293 (2025), https://doi.org/10.1016/j.compositesb.2025.112131.
[62] J.J.M. Machado, E.A.S. Marques, R.D.S.G. Campilho, L.F.M. da Silva, Mode II fracture toughness of CFRP as a function of temperature and strain rate, Compos. Part B Eng. 114 (2017) 311–318, https://doi.org/10.1016/j.compositesb.2017.02.013.
[63] Test Method for Mixed Mode I-Mode II Interlaminar Fracture Toughness of Unidirectional Fiber Reinforced Polymer Matrix Composites 2022. doi:https://doi.org/10.1520/D6671_D6671M-22.
[64] Brussat TR CS and MS. Fracture Mechanics for Structural Adhesive Bonds, AFMCL TR-77-1 63. Glenwood, IL: 1977.
[65] HexPLy 8552 Data Sheet. www.hexel.com. Physical Properties. n.d.
[66] A. Yudhanto, M. Alfano, G. Lubineau, Surface preparation strategies in secondary bonded thermoset-based composite materials: a review, Compos. Part A Appl. Sci. Manuf. 147 (2021), https://doi.org/10.1016/j.compositesa.2021.106443.
[67] 3Scotch-Weld Structural Adhesive Film AF 163–2. n.d.
[68] F. Sun, B.R.K. Blackman, A DIC method to determine the mode i energy release rate g, the j-integral and the traction-separation law simultaneously for adhesive joints, Eng. Fract. Mech. 234 (2020), https://doi.org/10.1016/j.engfracmech.2020.107097.
[69] F. Ramezani, M.R. Ayatollahi, A. Akhavan-Safar, L.F.M. da Silva, A comprehensive experimental study on bi-adhesive single lap joints using DIC technique, Int. J. Adhes. Adhes. 102 (2020) 102674, https://doi.org/10.1016/J.IJADHADH.2020.102674.
[70] R.D.S.G. Campilho, L.F.M. da Silva, Mode I Fatigue and Fracture Behaviour of Adhesively-Bonded Carbon Fibre-Reinforced Polymer (CFRP) Composite Joints, in: Fatigue and Fracture of Adhesively-Bonded Composite Joints, Elsevier Inc., 2015, pp. 93–120, https://doi.org/10.1016/B978-0-85709-806-1.00004-5.
[71] P. Davies, Influence of ENF specimen geometry and friction on the mode II delamination resistance of carbon/PEEK, J. Thermoplast. Compos. Mater. 10 (1997) 353–361, https://doi.org/10.1177/089270579701000404.
[72] I. De Baere, S. Jacques, W. Van Paepegem, J. Degrieck, Study of the mode i and mode II interlaminar behaviour of a carbon fabric reinforced thermoplastic, Polym. Test. 31 (2012) 322–332, https://doi.org/10.1016/j.polymertesting.2011.12.009.
[73] Y. Gong, Y. Hou, L. Zhao, W. Li, J. Zhang, N. Hu, A modified mode i cohesive zone model for the delamination growth in DCB laminates with the effect of fiber bridging, Int. J. Mech. Sci. 176 (2020), https://doi.org/10.1016/j.ijmecsci.2020.105514.
[74] M.M. Shokrieh, M. Salamat-talab, M. Heidari-Rarani, Dependency of bridging traction of DCB composite specimen on interface fiber angle, Theor. Appl. Fract. Mech. 90 (2017) 22–32, https://doi.org/10.1016/j.tafmec.2017.02.009.
[75] R. Lopes Fernandes, S. Teixeira de Freitas, M.K. Budzik, J.A. Poulis, R. Benedictus, From thin to extra-thick adhesive layer thicknesses: fracture of bonded joints under mode i loading conditions, Eng. Fract. Mech. 218 (2019), https://doi.org/10.1016/j.engfracmech.2019.106607.
[76] B.R.K. Blackman, A.J. Brunner, J.G. Williams, Mode II fracture testing of composites: a new look at an old problem, Eng. Fract. Mech. 73 (2006) 2443–2455, https://doi.org/10.1016/j.engfracmech.2006.05.022.
[77] H. (Hannah) Liu, G. Qi, G. Renaud, G. Li, C. (Lucy) Li, Application of the effective crack length method to model delamination of unidirectional composite laminates under mode II shear loadings, Compos. C: Open Access 12 (2023), https://doi.org/10.1016/j.jcomc.2023.100401.
[78] L.C. Zhao, L. Yuan, Z.R. Wang, Influence of 3D printing parameters on the fracture behavior of adhesive joints under mode II quasi-static loading: experimental and numerical insights, J. Adhes. (2025), https://doi.org/10.1080/00218464.2025.2602654.
[79] A.J. Kinloch, Adhesion and Adhesives, Springer Netherlands, Dordrecht, 1987, https://doi.org/10.1007/978-94-015-7764-9.
[80] B.F. Sørensen, T.K. Jacobsen, Determination of cohesive laws by the j integral approach, Eng. Fract. Mech. 70 (2003) 1841–1858, https://doi.org/10.1016/S0013-7944(03)00127-9.
[81] Dassault Systèmes Simulia Corp. S. ABAQUS/CAE 2024.
[82] I. Manoj, A. Kumar Shah, A. Jain, Strength and failure assessments of 3D printed PLA single lap joints: experimental and numerical analysis, Eng. Fail. Anal. 161 (2024), https://doi.org/10.1016/j.engfailanal.2024.108257.
[83] I. Manoj, A. Jain, Fracture behavior and strength enhancement of 3D-printed stepped-lap bonded joints using geometrically graded interfaces: experimental validation and damage modelling, J. Adhes. Sci. Technol. (2025) 1–31, https://doi.org/10.1080/01694243.2025.2575812.
[84] C.G. Dávila, S. Weeks, M. Czabaj, Propagation rate transients in j-controlled fatigue characterization of adhesives, Int. J. Fatigue 185 (2024), https://doi.org/10.1016/j.ijfatigue.2024.108377.
[85] Wanthal S, Schaefer J, Justusson B, Hyder I, Engelstad S, Rose C. Paper Number: Session Topic: Verification & Validation of Progressive Damage/Failure Analysis for Stiffened Composite Structures Title: Verification and Validation Process for Progressive Damage and Failure Analysis Methods in the NASA Advanced Composites Consortium. n.d.
[86] M. Toolabi, B.R.K. Blackman, Guidelines for selecting the dimensions of adhesively bonded end-loaded split joints: an approach based on numerical cohesive zone length, Eng. Fract. Mech. 203 (2018) 250–265, https://doi.org/10.1016/j.engfracmech.2018.05.019.
[87] F. Sun, R. Zhang, B.R.K. Blackman, Determination of the mode i crack tip opening rate and the rate dependent cohesive properties for structural adhesive joints using digital image correlation, Int. J. Solids Struct. 217–218 (2021) 60–73, https://doi.org/10.1016/j.ijsolstr.2021.01.034.
[88] M.L. Benzeggagh, M. Kenane, Measurement of mixed-mode delamination fracture toughness of unidirectional glass/epoxy composites with mixed-mode bending apparatus, Compos. Sci. Technol. 56 (1996).